

1 **Revision 1**

2 **Solving the Iron Quantification Problem in Low kV EPMA: An essential step toward**  
3 **improved analytical spatial resolution in electron probe microanalysis. I. Olivines**

4  
5 Aurélien Moy<sup>1,\*</sup>, John Fournelle<sup>1</sup> and Anette von der Handt<sup>2</sup>

6 <sup>1</sup>. Department of Geoscience, University of Wisconsin, Madison, WI 53706, USA.

7 <sup>2</sup>. Department of Earth Sciences, University of Minnesota, Minneapolis, MN 55455, USA.

8 \*Corresponding author. Email: [amoy6@wisc.edu](mailto:amoy6@wisc.edu)

9  
10 **ABSTRACT**

11  
12 The relatively recent entry of field emission electron microprobes into the field of  
13 microanalysis provides another tool for the study of small features of interest (e.g., mineral and  
14 melt inclusions, exsolution lamellae, grain boundary phases, high-pressure experimental  
15 charges). However, the critical limitation for accurate quantitative analysis of these  
16 submicrometer- to micrometer-sized features is the relationship between electron beam potential  
17 and electron scattering within the sample. In order to achieve submicrometer analytical volumes  
18 from which X-rays are generated, the beam accelerating voltage must be reduced from 15-20 kV  
19 to  $\leq 10$  kV (often 5 to 7 kV) to reduce the electron interaction volume from  $\sim 3$   $\mu\text{m}$  to  $\sim 0.5$   $\mu\text{m}$  in  
20 common geological materials. At these low voltages, critical  $K\alpha$  X-ray lines of transition  
21 elements such as Fe are no longer generated, so L X-ray lines must be used. However, applying  
22 the necessary matrix corrections to these L lines is complicated by bonding and chemical peak  
23 shifts for soft X-ray transitions such as those producing the Fe  $L\alpha$  X-ray line. It is therefore

24 extremely challenging to produce accurate values for Fe concentration with this approach. Two  
25 solutions have been suggested, both with limitations. We introduce here a new, simple and  
26 accurate solution to this problem, using the common mineral olivine as an example. We also  
27 introduce, for the first time, olivine results from a new analytical device, the Extended Range  
28 Soft X-ray Emission Spectrometer.

29 Keywords: EPMA, Olivine, Low kV, Iron, Microprobe, SXES, EMPA.

30

31

## INTRODUCTION

32

33 The electron probe microanalyzer (a.k.a., electron microprobe) has been an invaluable  
34 tool for Earth and planetary science since 1958, when its inventor Raimond Castaing and  
35 researcher Fredriksson (1958) determined that tiny (<60  $\mu\text{m}$ ) spherules found in deep sea  
36 sediments were in fact extra-terrestrial, by matching spherule compositions to the unique Fe:Ni  
37 signature of iron meteorites. Over the intervening five decades, the electron microprobe has been  
38 essential in virtually every aspect of geochemistry, mineralogy and petrology of both terrestrial  
39 and extra-terrestrial materials.

40 Electron microscopes and microprobes traditionally have used bent tungsten wire  
41 filaments as their beam source (and occasionally LaB<sub>6</sub>). Over the past decades, many scanning  
42 electron microscopes (SEM) and transmission electron microscopes (TEM) have switched to  
43 cold field emission (FE) gun beam sources. These FE electron sources provide brighter beams  
44 (smaller diameter, higher electron flux) relative to the traditional sources (Vladár and Postek  
45 2009), making images from FE SEMs significantly sharper and providing higher spatial  
46 resolution images. However, the long-term instability of cold-emission sources makes them

47 inadequate for the demands of quantitative analysis. The advent of thermal Schottky emission-  
48 type sources, which facilitate similarly small beam diameters but are more stable, represents a  
49 key advance that enables not only equivalent imaging to FE SEMs but higher spatial resolution  
50 quantitative analysis than traditional electron microprobes.

51 An example is given in Figure 1, where a secondary electron image (SEI) of an iron  
52 oxide crystal in NIST glass K409 (described in Fournelle et al. 2016) was taken with a JEOL  
53 JXA-8530FPlus electron microprobe. Here, the beam diameter can be determined using the  
54 edge resolution technique as described by Barkshire et al. (2000): the beam diameter  
55 corresponds to the distance over which some percentage change in signal intensity occurs in a  
56 scan over a sharp edge between two features. For the line crossing the interface in Figure 1a,  
57 the associated image intensity values are given in Figure 1b. Optimally, the adjacent dark and  
58 bright areas are "flat". However, in reality there are edge effects in many instances, so an error  
59 function is fit to normalize each of the darker and brighter regions. Traditionally, the image  
60 resolution or "beam diameter", is defined as the distance over which there is a signal rise from  
61 either 10 to 90%, 16 to 84%, or 25 to 75%. Following this convention, the beam diameter  
62 could be defined correspondingly as 38, 58, or 72 nanometers. Current usage seems to prefer  
63 the intermediate 16-84% rise (International Organization for Standardization, 2003).

64 However, even if electron images can be acquired with 10s to 100s of nanometer spatial  
65 resolution, the fact that an electron beam is generated by a field emission source does not change  
66 the fundamental physical processes by which electrons are scattered within the specimen and  
67 from which X-rays are generated. Indeed, to accurately probe small features, e.g. small  
68 inclusions, it is important to have a good estimate of the X-ray lateral resolution achievable. This

69 concept is not only governed by the beam size but also the electron ionization range, through the  
70 beam potential.

71 Typically, although not exclusively, Earth science researchers operate electron  
72 microprobes at gun voltages of 15 kV<sup>1</sup> for silicates, carbonates, phosphates, etc., and 20 kV for  
73 sulfides (and either voltage for metal oxides). These electron beam voltages result in electron  
74 scattering interaction volumes on the order of 2 to 3  $\mu\text{m}$ , with the primary X-rays generated  
75 within these volumes being much too large for many small features of interest.

76

### 77 **Monte Carlo Modelling of X-ray Generation**

78 To estimate the X-ray lateral resolution in addition to the beam diameter, the electron  
79 ionization range must be estimated. Analytical expressions aimed at calculating this electron  
80 ionization range were developed since the beginning of the electron microprobe era (Castaing  
81 1960; Duncumb 1960; Anderson and Hasler 1966; Reed 1966) up to recently (Hovington et al.  
82 1997; Merlet and Llovet 2012). However, Fournelle et al. (2016) showed that these models have  
83 limitations, especially for low accelerating voltages.

84 Another approach to estimating X-ray lateral resolution is to create a Monte Carlo  
85 simulation, wherein a large number of “random walks” of high energy electrons impinge upon  
86 and penetrate a specified material of a given geometry, and the occurring physical processes (e.g.,  
87 elastic and inelastic scattering, inner shell ionization, photoelectric absorption) are included in

---

<sup>1</sup> The physical terms kV and keV are used here in the strict sense: kV refers to an electrical potential (as between the cathode and anode of the source), whereas keV refers to an energy of a "particle" such as an electron or photon.

88 the computer codes. The speed of the simulation scales with the degree of simplification and  
89 approximation utilized. Three freely available programs of note are CASINO (Hovington et al.  
90 1997), DTSA-II (Ritchie 2011), and PENEPMA/PENELOPE (Salvat et al. 2013). Many  
91 microanalysts utilize these simulations to estimate the interaction volume for particularly small  
92 sized features of interest prior to setting the appropriate beam energy for EPMA operation.

93 The Monte Carlo simulation shown in Figure 2 illustrates that the electron beam energy  
94 is the primary factor in determining the size of the zone where X-rays are produced, not the  
95 electron beam source whether it be tungsten, LaB<sub>6</sub> or field emission source. The outer contour  
96 represents where the generation of Mg K $\alpha$  X-rays in an Fo80 olivine is only 1% of the maximum  
97 produced intensity from a 15 kV source. This contour is only slightly smaller for the field  
98 emission source, slightly less than 2  $\mu\text{m}$  laterally, compared to approximately 2.2  $\mu\text{m}$  laterally  
99 for the tungsten source—the difference being approximately equal to the proportional difference  
100 in beam diameters (under the general assumption that the electron beam has a Gaussian  
101 distribution). It is worth noting that Figure 2 only describes the generation of the Mg K $\alpha$  X-rays  
102 and does not take matrix absorption effects into consideration. Indeed, because of the absorption  
103 of the X-rays leaving the sample, the emitted X-ray generation volume will be slightly different  
104 from the generated X-ray production (or ionization range) volume.

105 Fournelle et al. (2016) showed that estimates of the ionization range by Monte Carlo  
106 simulation programs (in particular PENEPMA) matched those of experiments well when using  
107 a limited set of experimental data at 5 and 7 kV. This corroborates the usefulness of the Monte  
108 Carlo simulations to predict the analytical spatial resolution of EPMA measurements.

109

## 110 **Decreasing the Accelerating Voltage**

111            Since the 1960s, it has been understood that to reduce the electron interaction in electron  
112 probe microanalysis volume – that is, to achieve greater spatial resolution – the accelerating  
113 voltage must be lowered (Anderson 1967).

114            Monte Carlo simulations (Figure 3) demonstrate the critical importance of reducing the  
115 accelerating voltage from 15 kV down to less than half of that. Considering again an Fo80  
116 olivine, the PENEPMA Monte Carlo simulations suggest that the electron interaction volumes  
117 for both tungsten and FE sources are significantly reduced. Using the 99% criterion, the tungsten  
118 Mg K $\alpha$  lateral width drops from  $\sim 2.2 \mu\text{m}$  to  $\sim 800 \text{ nm}$  when going from 15 to 7 kV. The maximum  
119 depth decreases from  $\sim 1.6 \mu\text{m}$  to  $\sim 500 \text{ nm}$  and there is a similar reduction for FE lateral width,  
120 from  $\sim 1.75 \mu\text{m}$  to  $\sim 600 \text{ nm}$ ; and depth from  $\sim 1.5 \mu\text{m}$  to  $\sim 400 \text{ nm}$ .

121            It is worth noting that at very low accelerating voltage or at very low overvoltage  
122 (depending on the X-ray line studied) and depending on the density and composition of the  
123 material analyzed, the diameter of the X-ray generation volume may approach the diameter of  
124 the electron beam. In such a case, the beam diameter, and thus the electron source type, will have  
125 a major influence on the size of the X-ray lateral spatial resolution.

126

127            These simulations show that the key factor for improved analytical spatial resolution is  
128 the accelerating voltage rather than the electron beam size. However, we would like to note  
129 several things here: (1) FE imaging in the electron probe can provide the researcher with a more  
130 critical view for "targeting" the material to be probed, illuminating inclusions too small to be  
131 analyzed, but useful to avoid when focusing upon the host material, such as microlites in volcanic  
132 glass (Ken Severn, pers. comm.) (2) The previous Monte Carlo simulations assume a uniform  
133 distribution of the electron beam density. It is possible that the FE source may have a denser

134 electron density in the central core compared to the traditional Gaussian-shape of the tungsten  
135 and LaB<sub>6</sub> filaments, so that it may feasibly be possible to qualitatively image (X-ray map) at a  
136 tighter spatial resolution, while not enough for full quantitation. (3) The FE high electron density  
137 impacting the specimen can produce more damage than that from the tungsten filament, and in  
138 many cases operators of FE instruments (especially for geological materials) end up defocusing  
139 the beam—resulting in no gain in analytical spatial resolution compared with tungsten filament  
140 instruments. On the other hand, the FE's beam diameter remains smaller than from the  
141 comparable W source at high beam currents, and doesn't dramatically increase at low kV, giving  
142 the operator a choice of smaller achievable beam diameters relative to W instruments. (4) There  
143 are anecdotal accounts of FE sources lasting for 5-10 years, so that the higher cost of the tip is  
144 more than offset relative to frequent replacements of tungsten tips, with long uninterrupted  
145 service. Thus, pros and cons must be weighed when making a purchasing decision for a new  
146 instrument.

147

148 Another factor affecting spatial resolution in EPMA is secondary fluorescence: X-rays  
149 generated, not by the incident high energy electrons, but by both characteristic and continuum  
150 X-rays. These secondary fluoresced X-rays can be generated from tens to hundreds of  
151 micrometers away, though are primarily a problem for trace element analysis in normal 15 to 20  
152 kV EPMA. But for small, micrometer and sub-micrometer features, the "other" phase is very  
153 close and must be considered. Operation at low kV reduces this effect somewhat as the high-  
154 energy characteristic X-rays (and the high-energy bremsstrahlung photons), the major source of  
155 production of secondary fluorescence X-rays, are no longer created. However, lowering the  
156 accelerating voltage does not completely eliminate this effect. Monte Carlo programs such as

157 PENEPMMA/PENELOPE have the ability to model the extent of secondary fluorescence and also  
158 provide the ability to correct for it.

159

### 160 **Problems of low kV EPMA**

161 It is clear that lowering the kV is important to achieve increased spatial resolution in  
162 EPMA (regardless of electron source). However, there are two main issues which became  
163 important when considering operating at low kV: (1) X-ray lines generated and used at higher  
164 kV may no longer be available at lower kV, for example, the important element iron (the critical  
165 excitation energy for Fe K $\alpha$  is 7.114 keV (Zschornack 2007)); and (2) because the electrons no  
166 longer penetrate deeply into the material, the state of the sample surface becomes more critical:  
167 the smoothness of surface polish, the surface fidelity and cleanliness, and the conductive coating  
168 (of both the unknown and the standard). And because the beam no longer penetrates nor spreads  
169 out radially as much, there is much more concentrated energy in a smaller region, and sample  
170 damage can be magnified significantly. These issues are discussed in several recent publications,  
171 e.g., Kearns et al. 2014; Saunders et al. 2014. However, we focus here upon the first issue, the  
172 problem of the L lines of a critical transition metal, iron, in a common rock forming mineral,  
173 olivine.

174

175 Olivine was studied for two reasons: one, it is a relatively simple mineral phase,  
176 consisting dominantly of iron, magnesium, silicon and oxygen but showing a wide compositional  
177 range. Second, olivine is a key constituent in the Earth's mantle and crustal rocks as well as extra-  
178 terrestrial materials. EPMA analysis of small olivine grains or with complex zoning such as



179 found in chondrules (Libourel and Portail 2018) or in diffusion and grain growth studies (Shea  
180 et al. 2015) might necessitate working at low kV to achieve the desired spatial resolution.

181

182

183

#### 184 **The problem of low kV EPMA of iron-bearing materials**

185 It has been shown that it is difficult to do accurate EPMA with the  $L\alpha$  lines of the  
186 transition metals using the traditional matrix corrections (ZAF, phi-rho-Z), e.g., Llovet et al.  
187 (2012), Gopon et al. (2013), and Buse and Kearns (2018). The reasons include peak shape  
188 changes and position shifts due to differences in bonding between the standard and the  
189 unknowns, as well as problems with the accuracy of mass absorption coefficients (MACs), with  
190 the  $L\alpha$  peak lying directly across the absorption edge. There is a major increase in the MAC for  
191 Fe  $L\alpha$  by Fe from right before the edge at 710 eV (Zschornack 2007), with a value of  $\sim 2180$   
192  $\text{cm}^2/\text{g}$  at 704 eV (Heinrich 1987) to past the edge, with a value of  $\sim 14400 \text{ cm}^2/\text{g}$  at 717 eV  
193 (Heinrich 1987). This complex situation causes varying "self absorption" yields for different  
194 MACs for the same element for different Fe-bearing compounds—which is not the case for the  
195 MAC of the Fe  $K\alpha$  X-ray line by atoms of Fe.

196 Gopon et al. (2013) found that the “non-traditional”  $L\ell$  ("el el", L3-M1 transition) for Fe  
197 could be successfully utilized for quantification as it lay far from any Fe absorption edge. The  
198 use of the  $L\ell$  line of Fe compared to the  $L\alpha$  line works well for iron silicides but its lower relative  
199 count rates in many minerals and glasses of interest to geoscientists leads to diminished statistical  
200 precision. To compensate for the low X-ray intensity of the Fe  $L\ell$  line, measurements require  
201 longer counting times or the use of a monochromator crystal with a high detection efficiency. In

202 addition, the Fe L $\ell$  line partially interferes with the Fe L $\alpha$  line and the second order of diffraction  
203 of the Mg K $\alpha$  X-ray line. Therefore, the accuracy of quantification using the Fe L $\ell$  line in  
204 olivines at low to moderate Fe concentrations is increasingly dependent on the magnitude of the  
205 interference correction for Mg. Also, even though the L $\ell$  line originates from a transition  
206 between “inner” electron shells, recent studies by Terauchi and Sato (2018) show that the Fe L $\ell$   
207 line peak position can shift between different iron oxides and then, potentially, between other  
208 iron compounds. Thus, it would be desirable if the analytical problems of the L $\alpha$  line could be  
209 resolved as to enable its use in low kV EPMA. Llovet et al. (2016) found that for the transition  
210 metal Ni, if an empirical correction was applied to the fluorescence yield (a fundamental  
211 parameter in the matrix correction) of the Ni L $\alpha$  X-ray line, in addition to the reevaluation of the  
212 Ni L $\alpha$  MAC by atoms of Ni, there was an improvement in the matrix-corrected results.  
213 Following this methodology, Buse and Kearns (2018) recently evaluated the use of the Fe L $\alpha$   
214 X-ray line for quantification of Fe in olivines in the compositional range between Fo91 and Fo0.  
215 They showed that it was possible to achieve very good results with relative deviations to the  
216 expected Fe concentrations varying from 1 to 5%, at least for the olivines with FeO content  $\geq$  16  
217 wt% (Buse and Kearns did not report quantification results using their method for olivines with  
218 lower FeO content). Their proposed method is to reevaluate the MACs of the Fe L $\alpha$  X-ray line  
219 by Fe in olivines at a given X-ray energy (or spectrometer position) as well as to evaluate partial  
220 fluorescence enhancement factors. Both factors vary smoothly with respect to the Fe  
221 concentration and can be interpolated using a regression fit. Thus, these coefficients can be used  
222 in ZAF or phi-rho-z matrix correction algorithms to quantify Fe using traditional k-ratios. The  
223 reference material (i.e. standard) they utilized for this approach was an Fo33 olivine from  
224 Dabbahu Volcano (Ethiopia), provided by a researcher at their institution. However, because of

225 the proximity of the Fe L<sub>2</sub> and L<sub>3</sub> absorption edges which lead to a rapid increase of the MAC  
226 with increasing X-ray energy, determining these coefficients using the described method can  
227 lead to close but different values of the MAC measured by different instruments/spectrometers  
228 due to differences on the resolution of the spectrometers used. To apply their proposed method,  
229 one will have to re-determine the MACs on their own instrument/spectrometers and a set of  
230 olivines reference materials. In addition, matrix correction algorithms allowing the use of  
231 different MAC values for the unknown and for the standard, in addition to the use of user-defined  
232 partial fluorescence yields, are not broadly available yet, making it difficult to utilize this method  
233 for routine applications.

234

235

236

## MATERIALS AND METHODS

237

### 238 **Electron Probe Measurements**

239 The spectra of the Fe L $\alpha$ -L $\beta$  X-ray lines were measured at the Eugene Cameron electron  
240 microscopy laboratory, Department of Geoscience, University of Wisconsin-Madison, using a  
241 CAMECA SXFiveFE electron microprobe, and at the Department of Earth Sciences, University  
242 of Minnesota using a JEOL JXA-8530FPlus electron microprobe. Both instruments used Probe  
243 for EPMA to collect the data (Donovan et al. 2018).

244 The JEOL JXA-8530FPlus is outfitted with the new Soft X-ray Spectrometer “SXES”  
245 that consists of an extended range diffraction grating JS2000, and a Peltier-cooled CCD camera  
246 (Terauchi et al. 2011). This type of spectrometer acquires the whole spectrum between 240 and  
247 2800 eV simultaneously (similar to a SiLi or SDD EDS but with high spectral resolution).

248 Three wavelength-dispersive spectrometers (WDS) were used to record the spectra on  
249 the SXFiveFE microprobe and two WDSs and the SXES were used on the JXA-8530FPlus  
250 microprobe (further details including monochromators used are given in Supplemental materials,  
251 Table I). All the spectrometers have a takeoff angle of 40°.

252

253 On the CAMECA instrument, 4 spectra covering the Fe  $L\alpha$ - $L\beta$  spectral range were  
254 acquired on each sample and then averaged together. The spectra were measured at 7 kV and 90  
255 nA, from 0.686 keV to 0.734 keV with 500 steps and a dwell time of 1.8 seconds/step for the  
256 TAP crystals and 1.5 seconds/step for the PC0 pseudocrystal.

257 On the JEOL instrument, 3 spectra were accumulated for each sample with the WDS's  
258 and only one spectrum was recorded with the SXES, as this last detector is much more counting-  
259 efficient than the WDS. With the WDSs, the spectra were recorded from 0.688 keV to 0.732 keV  
260 with 500 steps and a dwell time of 2.4 seconds/step. With the SXES, the spectra were recorded  
261 at 7 kV and 20 nA, from 0.236 to 2.830 keV with 4096 steps and a total counting time of 15  
262 minutes. A 5  $\mu\text{m}$  beam diameter was used for all the measurements on both electron microprobes.

263 The integrated areas of the spectra were calculated by numerical analysis using the  
264 trapezoidal rule. For the spectra recorded with the SXES detector, the step size is relatively large  
265 compared to the width of the X-ray lines. This implies a small underestimation of the calculated  
266 area using this spectrometer. The small error resulting from this underestimation will be partially  
267 cancelled out, and thus minimized, during the calculation of the area k-ratio as the Fe  $L\alpha$ - $L\beta$  X-  
268 ray line shapes of the olivine samples and of the Fe standard are very similar. Before the  
269 determination of the area integral, the background was fitted and removed using a linear curve  
270 for the TAP crystals and the SXES, and using an exponential background for the PC0 crystal.

271 One concern that arises when measuring Fe in Fe-bearing materials using an electron  
272 beam is the change of the oxidation state of Fe due to interactions with the incident electrons.  
273 The change of Fe oxidation state under beam irradiation can lead to inaccuracies when measuring  
274 the X-ray intensity at the peak maximum or can lead to distortion of the recorded spectrum and  
275 it has been shown that the Fe peak position will shift toward the high energies when the oxidation  
276 state changes from Fe<sup>2+</sup> to Fe<sup>3+</sup> (Fialin et al. 2011). In olivine, which contains almost exclusively  
277 divalent Fe, such a change in the oxidation state is unlikely to occur but must be investigated  
278 nevertheless. A recent paper by Li et al. (2019) reports a method to observe the change in Fe  
279 oxidation by monitoring the variations of the X-ray intensity ratio FeL $\beta$ /FeL $\alpha$  over time. We  
280 have monitored the FeL $\alpha$  and FeL $\beta$  X-ray intensities at 15 kV, 90 nA for 260 seconds with  
281 measurements at 10 second intervals on synthetic fayalite, Wards fayalite and San Carlos olivine.  
282 The measurements were repeated at least 3 times on different locations and then averaged. No  
283 obvious change in the FeL $\beta$ /FeL $\alpha$  ratio was observed (see Supplementary materials, Figure 1).  
284 This indicates that the Fe oxidation state in olivine is not altered by the electron beam.

285  
286 **Olivines**

287 A set of nine olivine samples was used in this study. The intermediate Fe range (Fo47-  
288 73) is covered by five olivines from (Aleutian) Shishaldin Volcano basalts (Fournelle 1988) and  
289 two olivines from the Smithsonian National Museum of Natural History: the Springwater olivine  
290 is from the microbeam standards collection (USNM 2566, Jarosewich et al. 1980) and the San  
291 Carlos is a "coarse" fraction from the same split as the USNM 111312/444 in the microbeam  
292 standards collection (T. Rose, pers. comm.). The synthetic fayalite source (Finch et al. 1980) was  
293 Jill Banfield. The Wards fayalite is a sample from Crystal Park, Colorado (Barker et al. 1975).

294           These olivines' iron elemental concentrations range from 7.64 wt% to 53.9 wt%. The  
295 olivine samples were characterized by EPMA at 15 kV and 20 nA, using the traditional  $K\alpha$  X-  
296 ray lines, the PAP matrix correction algorithm (Pouchou and Pichoir 1991), and the MAC30  
297 mass absorption coefficients (Heinrich 1987). At least 15 points were acquired to reduce the  
298 statistical uncertainties. The instrument used to measure the composition was a CAMECA SX51  
299 microprobe at the Eugene Cameron electron microscopy laboratory, Department of Geoscience,  
300 University of Wisconsin-Madison, equipped with five WDSs. The details of the oxide  
301 composition of each sample are given in Table I (and the corresponding stoichiometric formula  
302 are given in Supplemental materials, Table II). As further results of this paper are given in  
303 elemental wt%, those concentrations of Fe are also shown in Table I. Particular attention was  
304 paid to select one homogeneous crystal (determined by BSE imaging and multiple EDS  
305 measurements) from each sample, and to focus on the same area for both the 15 and the 7 kV  
306 measurements.

307

### 308 **Carbon contamination**

309           To study and mitigate the effects of carbon contamination during spectra acquisition, a  
310 custom cryo-chiller replacing the liquid nitrogen dewar used to cool the CAMECA cold plate  
311 was used to perform the measurements on the CAMECA SXFiveFE instrument. This  
312 anticontamination device was able to decrease the temperature in the microprobe chamber to  
313 about  $-150^{\circ}\text{C}$  and reduced the vacuum to as low as  $8 \times 10^{-7}$  Pa. In addition to freezing the volatile  
314 contaminants, the cryo-chiller also cooled the samples by radiative transfer, reducing the  
315 mobility of contaminants on the sample surface.

316 To study the effects of carbon contamination on the measurements, long spectrum  
317 acquisitions (~19 minutes for each spectrum) were performed first by recording the spectrum  
318 from low X-ray energies to high X-ray energies and then by repeating the measurements from  
319 high to low X-ray energies on a new spot. Any significant amount of carbon contamination  
320 deposited during spectrum acquisition should distort the spectrum by decreasing the electron  
321 landing energy and increasing the absorption of the emitted X-rays. These effects, more  
322 pronounced at the end of the acquisition than at the beginning, should result in different  
323 appearances between the two spectra.

324 Spectrum acquisitions were performed on pure Fe, USNM Spring Water olivine, San  
325 Carlos olivine, Wards fayalite and synthetic fayalite, covering the entire range of Fe  
326 concentrations. The measurements were performed at 7 kV and 90 nA using three WDSs (LTAP,  
327 TAP and PC0 monochromator crystals as described in Supplementary materials, Table I). X-  
328 rays were recorded with 100 steps and for photon energies ranging from 685.8 to 733.7 eV for  
329 the LTAP crystal, from 684.8 to 732.7 eV for the TAP crystal, and from 582.5 to 892.3 eV for  
330 the PC0 crystal. Three different spectra were measured on each sample and each direction and  
331 averaged together (the averaged spectra are shown in Supplementary materials, Figure 2).

332 The spectra measured in both directions show no significant differences in peak shape or  
333 intensities on either the background or the tails of the peaks. The only noticeable differences are  
334 slightly less intense peak maxima for the  $L\alpha$  line and more intense maxima for the  $L\beta$  line when  
335 the spectrum was recorded from high to low energies relative to the other direction. This  
336 difference is well explained by an increase of the carbon contamination thickness during  
337 acquisition. However, the differences between the spectra are typically within the uncertainties  
338 of the counting statistics associated with the measurements. The maximum relative standard

339 deviation (RSD) of the calculated areas of the Fe  $L\alpha$ - $L\beta$  X-ray lines between spectra measured  
340 in opposite directions was found to be 1.8% for the Spring Water olivine (low Fe concentration)  
341 when measured with the TAP crystal (low detection efficiency, large statistical fluctuations).  
342 Nevertheless, all data used to derive the calibration curves came from the spectra measured with  
343 increasing spectrometer positions, i.e. with decreasing photon energy (except for the SXES  
344 where this is not relevant) to be consistent.

345         The changes in peak area due to carbon contamination remain generally very small, with  
346 mean RSD found to be 0.8%, 1.3% and 0.4% for the LTAP, TAP and PC0 monochromator  
347 crystals, respectively. This indicates carbon contamination has no significant effect on the  
348 measurements when using a cryo-chiller at these experimental conditions. No cold trap or other  
349 anti-contamination devices were used in the JEOL JXA-8530FPlus instrument or, later, in the  
350 CAMECA SX51 instrument. However, the obtained results (the area k-ratios) agree within the  
351 uncertainties with the results obtained on the CAMECA SXFiveFE instrument using the cryo-  
352 chiller. This indicates that even when no anticontamination devices are used, carbon  
353 contamination effects are not significant enough to significantly affect the measurements.

354

355

## RESULTS

356

357         We studied utilization of the Fe  $L\alpha$  line for low kV EPMA in a set of olivines as well as  
358 a set of iron silicides (Moy et al. 2019). An essential part of this involved attempting to determine  
359 the Fe  $L\alpha$  MACs, which lead to a reevaluation of the procedures used to measure them. This  
360 reevaluation, going back to fundamental parameters, sheds light on why it is so difficult to



361 determine the correct MAC in the energy/wavelength region at the Fe  $L\alpha$  peak position, which  
362 lies across the Fe  $L_3$  edge position.

363 All measured X-ray peaks are broader than they would appear naturally: their shapes are  
364 considered to be Voigt profiles, convolutions of two broadening mechanisms, one being the  
365 Lorentzian profile for the natural width of the peak, the other the Gaussian profile for the  
366 broadening by the specific spectrometer being used (Rémond et al. 1993). However, direct  
367 determination of the MAC of the Fe  $L\alpha$  peak from an iron silicide or olivine was found to be  
368 impossible. Any attempt to measure precisely the MAC at any single peak channel is not possible  
369 because of the Gaussian broadening of the spectrometer and the rapidly changing MAC value  
370 under the energy range of this Gaussian. Ultimately, if it were possible to correctly measure the  
371 MACs for a range of iron-bearing phases, they would define a 3 dimensional plot, as functions  
372 of both specific energy/wavelength as well as Fe content. A full explanation and theoretical  
373 derivation proving the futility of determining MACs for Fe-bearing phases, using the traditional  
374 EPMA approach (e.g., XMAC (Pouchou 1996)) is given in Moy et al. (2019).

375

### 376 **Traditional quantification method with the Fe $L\alpha$ X-ray line**

377 To corroborate the need for an improved quantification method when using the Fe  $L\alpha$  X-  
378 ray line at 7 kV, we tried to quantify our set of olivines, previously characterized at 15 kV using  
379 the Fe  $K\alpha$  X-ray line and varying primary standards: (1) the pure Fe standard as it was used to  
380 perform the quantification using the  $K\alpha$  X-ray line, (2) the Wards fayalite standard as  
381 representative of commonly used Fe standards in EPMA for geological work, and (3) the SH111  
382 standard as the one with the highest Fe abundance and a substantial amount of Mg in our set of  
383 olivines. The quantification results, performed using the PAP matrix correction algorithm

384 (Pouchou and Pichoir 1991) and the MAC30 MAC data table (Heinrich 1987), are very poor  
385 (see Supplementary materials, Table III) and yield RSD of up to 60% compared to their nominal  
386 Fe concentration, as seen in Figure 4. The only adequate results are obtained when the Fe  
387 quantification of an olivine is performed using itself as a primary standard. These poor  
388 quantification results can be attributed to changes of the atomic parameters (MAC and  
389 fluorescence yield) between the different olivine and pure Fe samples. These parameters, in  
390 addition to not being known precisely except for pure Fe, will differ between the quantified  
391 olivine and the standard, and traditional matrix correction algorithms do not support different  
392 atomic values for the unknown and the standard. It is also worth noting that the RSD increases  
393 with increasing Fe content in the olivines at approximately the same rate, regardless of the  
394 standard used. These results show that quantification of Fe in olivines with the  $L\alpha$  X-ray line  
395 cannot be done using the traditional quantification method.

396

### 397 **Plot of Fe $L\alpha+L\beta$ k-ratio versus Fe content**

398 After much time and effort evaluating the Fe  $L\alpha$ - $L\beta$  spectra of both iron silicides and  
399 olivines, and realizing that there were insurmountable obstacles to determining the Fe  $L\alpha$  MACs  
400 correctly, another approach was called for. What to do? When in doubt, make a plot. And so,  
401 combined-integrated k-ratios were determined: we integrated the areas under the Fe  $L\alpha$ - $L\beta$   
402 wavescan peaks and subtracted the backgrounds, for both the experimental samples and a pure  
403 iron standard, and then created "area k-ratios" using the pure iron standard. When these  
404 integrated Fe  $L\alpha$ - $L\beta$  wavescan area k-ratios were plotted against the sample Fe-content (Figure  
405 5), a simple relationship became obvious (experimental k-ratios are given in Supplemental  
406 materials, Table IV).

407           There is a strong degree of direct correlation between the integrated Fe  $L\alpha+L\beta$  k-ratios  
408 and the Fe content of the olivines. The data can be fitted by a simple third order polynomial (with  
409 conditions of being 0 when the area k-ratio is 0 and being as close as possible to 100 when the  
410 area k-ratio is 1) with an  $R^2$  value of 0.999.

411

412           This simple approach allows the X-ray intensity of the integrated Fe  $L\alpha-L\beta$  peak to be  
413 used to quantify the iron content of olivines. We suggest it can be applied to any conventional  
414 electron microprobe; the only limitation is having a spectrometer takeoff angle of  $40^\circ$ , the  
415 accelerating voltage being 7 kV and the standard to calculate the k-ratio being pure Fe. It entails  
416 (a) the measurement of the area of Fe  $L\alpha-L\beta$  spectrum of the olivines being studied, (b) the same  
417 measurement on a pure Fe metal standard (a common, easily available standard), and removing  
418 the backgrounds for both the olivine and the Fe metal standard, and (c) using the following  
419 calibration curve (equation (1)) to read out the Fe wt% of the olivine:

420 (1)     $Fe\ wt.\ \% = 81.718 \times K + 134.07 \times K^2 - 115.79 \times K^3$

421 where K is the area Fe  $L\alpha+L\beta$  k-ratio. This elemental Fe value would then be input into the  
422 matrix correction software as a defined element, with the other elements quantified using the  
423 traditional matrix correction.

424

425

426

## DISCUSSION

427

428    **Theoretical derivation of area k-ratio**

429 Why would this apparently simple calibration curve work, and we assert, work on any  
430 electron microprobe? To understand this, we enter the realm of the physics used to go from the  
431 raw X-ray intensities, via the so-called “matrix correction”, to the final corrected element values.  
432 Most people delve as far as the so-called ZAF correction, which was a highly simplified  
433 expression needed when computing power was minimal. But it all rests upon a strong physical  
434 basis, the so-called fundamental equation of the microanalysis, which can be written as:

435

436 (2) 
$$I_X(E_{ph}) = C_A \frac{N_a}{A_r} n_{el} \omega_i^A \Gamma_{ij}^A Q_i^A(E_0) \int_0^\infty \varphi_i(\rho z) e^{-\frac{\mu(E_{ph}) \rho z}{\sin \theta_a}} d\rho z \left[ \varepsilon \frac{\Delta\Omega}{4\pi} \right] (E_{ph}) F (1 + g_{CK})$$

437

438 where  $I_X(E_{ph})$  is the number of characteristic X-rays of energy  $E_{ph}$  recorded per unit of time for  
439 the X-ray line of interest,  $C_A$  is the concentration of the studied element A,  $N_a$  is the Avogadro  
440 number and  $A_r$  is the atomic weight of element A.  $n_{el}$  is the number of primary electrons  
441 reaching the sample per unit of time,  $\omega_i^A$  is the fluorescence yield for the element A and a  
442 primary ionization in the shell i (i.e., the probability of emitting a photon during relaxation of  
443 atom A with an initial vacancy in the electronic shell i).  $\Gamma_{ij}^A$  is the transition rate from shell j to i  
444 (i.e., the probability that the relaxation occurs by the transition of an electron from the shell j to  
445 the vacancy located in shell i).  $Q_i^A(E_0)$  is the ionization cross section (in  $\text{cm}^2$ ) of the shell i of  
446 element A by impact of electrons with energy  $E_0$ .  $\varphi_i(\rho z)$  is the so-called phi-rho-z function  
447 representing the depth distribution of ionization of electronic shell i of element A at mass depth  
448  $\rho z$  inside the sample for an incident electron beam of energy  $E_0$ . The next term in equation (2),  
449 corresponding to the exponential factor, represents the attenuation of the created X-rays inside  
450 the sample before they reach the surface with an angle  $\theta_a$  corresponding of the takeoff angle of

451 the detector.  $\frac{\mu}{\rho}(E_{ph})$  is the MAC (in  $\text{cm}^2/\text{g}$ ) of the sample for a photon of energy  $E_{ph}$ .  $\varepsilon$  and  $\frac{\Delta\Omega}{4\pi}$   
452 are the intrinsic detection efficiency of the spectrometer for photons of energy  $E_{ph}$  and the  
453 geometric detection efficiency of the spectrometer also for photons of energy  $E_{ph}$ , respectively.  
454  $F$  represents the secondary fluorescence enhancement factor ( $F \geq 1$ ) and the  $(1+g_{CK})$  factor  
455 represents the X-ray intensity enhancement by Coster-Kronig and super-Coster-Kronig effects.  
456 The X-ray intensity calculated by equation (2) corresponds to the intensity of a single  
457 characteristic X-ray. In the case where several characteristic lines are considered, the total X-ray  
458 intensity becomes the sum of the X-ray intensities of each of the considered lines, each intensity  
459 being calculated using equation (2) with the appropriate atomic parameters.

460 This equation works well in the general case, but it assumes some simplifications that  
461 can be problematic in certain circumstances. One drawback of this equation is the fact that the  
462 characteristic X-ray is supposed to be emitted at an exact energy  $E_x$ . In reality, the X-ray line has  
463 a natural width (also called natural broadening) following a Lorentzian shape for the inner shell  
464 transitions and with its maximum centered on  $E_x$ .

465 In addition, the spectrometer response function must also be taken into account. This  
466 function depends on the X-ray energy recorded ( $E_{ph}$ ). In the case of crystal monochromators,  
467 because of crystal imperfections such as mosaic misorientation (Bertin, 1975), the detector  
468 response function will not be a Dirac (delta) function following Bragg's law, i.e., not only the  
469 wavelength satisfying  $n\lambda = 2d \sin(\theta)$  will be reflected. Instead, wavelengths of radiation  
470 length  $\lambda + d\lambda$  will also be reflected but with a reduced intensity, which decreases rapidly as  $d\lambda$   
471 increases. The detector response function can be well described by a Gaussian function centered  
472 on the recorded wavelength  $\lambda_x$  (or on the recorded energy  $E_x$  in an energy representation) and  
473 characterized by a full width at half maximum  $\Gamma_G$ . When recording the X-rays at an energy  $E_{ph}$ ,

474 all the photons in a range  $[E_{ph}-3\Gamma_G; E_{ph}+3\Gamma_G]$  are appreciably reflected by the crystal, with an  
475 intensity proportional to the Gaussian function. With traditional WDS, the X-rays are usually  
476 detected by a flow gas detector or by a sealed gas detector. The response function of this detector  
477 is usually represented by an integrator: all the photons reaching the detector are detected, without  
478 discrimination of their energy. An energy window can be used to discriminate high order X-ray  
479 reflections (corresponding to higher energies) but cannot distinguish photons in an energy range  
480 as small as  $[E_{ph}-3\Gamma_G; E_{ph}+3\Gamma_G]$ .

481 The natural spectrum, i.e. the spectrum emitted from the sample before detection, is  
482 described by the product of the emitted intensities  $I_x$  with the area-normalized Lorentzian  
483 functions. The recorded spectrum is then the convolution of the natural spectrum with the  
484 spectrometer response function. More details are given in Moy et al. (2019). When  $I_x$  is not  
485 dependent on the X-ray energy, i.e. when  $\left[\varepsilon \frac{\Delta\Omega}{4\pi}\right](E_{ph})$  and  $\frac{\mu}{\rho}(E_{ph})$  are constant over the X-ray  
486 energy range effectively recorded by the spectrometer due to its instrumental broadening  
487 (typically from  $E_{ph}-3\Gamma_G$  to  $E_{ph}+3\Gamma_G$ ), the X-ray intensity can be extracted from the previously  
488 mentioned convolution product. Consequently, by normalizing the unknown intensity with an  
489 intensity recorded on a standard sample, and assuming that the natural broadening of the X-ray  
490 line and the spectrometer broadening are the same for both the unknown and the standard, the  
491 remaining convolution product will be the same for the unknown and the standard and will cancel  
492 out during the calculation of the so-called k-ratio. One can then obtain the k-ratio traditionally  
493 used to perform quantitative EPMA.

494 However, in the case of the Fe  $L\alpha$  and  $L\beta$  X-ray lines, the MAC changes rapidly over  
495 the spectrometer broadening energy range because of the nearby presence of the  $L_2$  and  $L_3$   
496 absorption edges (and can additionally vary due to different compositions and bonding

497 environments between the standard and the unknown), and so the X-ray intensity,  $I_X$ , cannot be  
498 extracted from the above-mentioned convolution—which is what is typically done in “normal  
499 EPMA”. The broadening effects now do not cancel out and so the measured k-ratio still depends  
500 on the spectrometer broadening, i.e. of the instrument used, and hence will not be suitable for a  
501 universal ZAF or phi-rho-Z matrix correction.

502 Fortunately, by integrating the intensity of the X-ray lines of interest over the whole  
503 energy range – theoretically from  $-\infty$  to  $+\infty$ , but in practice over the energy range of the Fe  $L\alpha$ -  
504  $L\beta$  spectrum where the characteristic X-ray intensity is not negligible – the integral of the  
505 convolution product can be separated into the product of two integrals:

506

$$507 \quad (3) \quad \int_{-\infty}^{+\infty} \int_{-\infty}^{+\infty} I_X(E)L(E) G(E - E_{ph}) dE dE_{ph} = \int_{-\infty}^{+\infty} I_X(E)L(E)dE \int_{-\infty}^{+\infty} G(E)dE$$

508

509 where  $L(E)$  and  $G(E)$  represent the Lorentzian (the natural broadening) and Gaussian (specific  
510 detector broadening) contributions to the spectrum, respectively. Notice that when several X-ray  
511 lines are considered,  $L(E)$  is replaced by a sum of Lorentzian functions corresponding to the  
512 different transitions, such as the Fe  $L\alpha_1$ , Fe  $L\alpha_2$  and Fe  $L\beta_1$  X-ray lines, at the condition that  
513  $I_X(E)$  is also replaced by a sum of X-ray intensities, each corresponding to the different  
514 transitions taken into account and each being calculated by means of equation (2) using the  
515 appropriate atomic parameters. Other transitions, far from those of interest, can be disregarded  
516 as we only calculate the area for the Fe  $L\alpha$ - $L\beta$  X-ray lines and they are not interfering with these  
517 lines of interest.

518

519 By calculating the k-ratios using the area of the X-ray lines (noted  $kr_{Area}$ ), where the  
520 superscript  $u$  is for the unknown and  $s$  is for the standard, we obtain:

521

522 (4) 
$$kr_{Area} = \frac{\int_{-\infty}^{+\infty} I_X^u(E)L(E)dE}{\int_{-\infty}^{+\infty} I_X^s(E)L(E)dE} \frac{\int_{-\infty}^{+\infty} G(E)dE}{\int_{-\infty}^{+\infty} G(E)dE} = \frac{\int_{-\infty}^{+\infty} I_X^u(E)L(E)dE}{\int_{-\infty}^{+\infty} I_X^s(E)L(E)dE}$$

523

524 The k-ratio in equation 4 is now independent of the spectrometer broadening and hence suitable  
525 for the creation of a universal calibration curve. The only limitation that remains is that the  
526 takeoff angle of the detector (included in the term  $I_X$ ) must be of  $40^\circ$ , as is the case for most of  
527 the commercially available electron microprobes today (in particular the JEOL and CAMECA  
528 instruments used in this study).

529

### 530 **Calibration Curve using the $L\alpha$ - $L\beta$ Area**

531 The integrated areas of the Fe  $L\alpha$ - $L\beta$  spectra measured on each olivine sample were  
532 normalized to the area integral obtained on the pure Fe standard (area k-ratio) and plotted as a  
533 function of the Fe concentration, shown previously in Figure 5.

534 The experimental data follow a smooth increase with increasing Fe concentration. We  
535 found that values are very similar from one spectrometer to another, independent of the  
536 spectrometer used, and in agreement with the theoretical treatment. Therefore, data across  
537 instruments and spectrometers were averaged subsequently. The averaged data was fitted by a  
538 third order polynomial under the physical conditions that the Fe concentration is equal to 0 when  
539 the area k-ratio value is 0 and equal to 1 when the area k-ratio value is 1. As shown in Figure 6,  
540 the resulting fit is very good with a with a regression factor of 0.999. While the data measured



541 on the SH111 and Wards fayalite olivine samples have the highest RSD, the values still agree  
542 with the fitting curve within the statistical uncertainties.

543

544

545

546

### 547 **Testing the Calibration Curve**

548 The quantification of olivines based on this new approach follows a two-step process:  
549 first the Fe concentration is determined with the area k-ratio calibration curve using Fe metal as  
550 a standard and then, fixing this Fe value in the matrix correction, the other elements are  
551 quantified using the traditional method with measured k-ratios.

552 The calibration curve was tested again on a subset of our olivine samples, but using  
553 different grains and using a different electron microprobe (CAMECA SX51 at the University of  
554 Wisconsin-Madison) and some additional olivines with good results. Each olivine grain was  
555 quantified again at 15 kV using the traditional Fe  $K\alpha$  X-ray lines prior to spectra acquisition to  
556 account for any inter-grain compositional variability. Three WDSs were tested: two TAP crystals  
557 ( $2d = 25.745 \text{ \AA}$ ) and a PC0 crystal ( $2d = 45.0 \text{ \AA}$ ). Comparisons of the nominal Fe concentrations  
558 measured at 15 kV with the Fe concentrations measured at 7 kV using the calibration curve are  
559 given in Table II and shown on Figure 7.

560

561 Very good results are obtained with the PC0 crystal with almost all the samples with the  
562 exception of the Rockport fayalite where Fe was underestimated by 2.28 wt%. Both TAP crystals  
563 gave reasonably good results for almost all the samples but also highly underestimate the Fe

564 concentration of the Rockport fayalite. This may indicate a problem with (1) the nominal  
565 composition of this sample (even if it has been re-acquired prior to the measurement, the spectra  
566 were acquired at close but different positions and local heterogeneities on the fayalite (Rose et  
567 al. 2009) can explain the seen deviations), (2) a tilt of the sample or sample holder, changing the  
568 takeoff angle, or (3) a problem with the calibration curve itself. The latter seems unlikely to be  
569 the explanation as for the PC0 crystal, the Fe composition of the Rockport fayalite samples are  
570 well reproduced and the calibration curve varies smoothly everywhere. The spectrometer number  
571 2 underestimated the Fe concentration in general, which can be attributed to its relatively low X-  
572 ray intensity yield (lower than for the two other spectrometers) making the recorded spectra  
573 noisier and therefore, making the background removal less accurate. An overestimation of the  
574 background leads to an underestimation of the peak area and then to an underestimation of the  
575 Fe concentration.

576

577 In addition, the calibration curve was also tested on a different set of olivines using the  
578 CAMECA SXFiveFE instrument, following the same experimental protocol and the obtained Fe  
579 concentration, in wt%, are given in Table III and plotted in Figure 8. The k-ratio versus nominal  
580 Fe concentration curve acquired on these samples is in very good agreement with the previously  
581 acquired calibration curve. Hence, the Fe concentrations determined using the calibration curve  
582 (Eq. 1) are also in good agreement with the expected concentration, as shown in Table III. Again,  
583 the determined Fe concentration for the fayalite samples is underestimated especially for the  
584 spectrometer number 2 which has the lowest detection efficiency. Except this deviation, other  
585 results are in very good agreement with the expected Fe concentrations, demonstrating the  
586 robustness of this analytical approach irrespective of instrument, spectrometer and crystal

587 choices. It is worth noting that the area calibration curve is also robust against the spectrometer  
588 energy drift (change of the maximum peak position over time) as the entire spectrum is recorded  
589 and integrated.

590

### 591 **Calibration Curve using the maximum intensity of the $L\alpha$ X-ray line**

592 The drawback of the area intensity method is the long acquisition time for each spectrum.  
593 The combination of the calibration curve approach with traditional k-ratios was tested as a means  
594 to shorten acquisition times. Intensity measurements using the SXFiveFE and SX51 instruments  
595 were acquired on the olivine samples at the maximum intensity of the Fe  $L\alpha$  X-ray line and on  
596 each side of the Fe  $L\alpha$ - $L\beta$  peaks (at 0.686 keV and 0.733 keV for the LTAP and TAP crystals  
597 and at 0.583 keV and 0.830 keV for the PC0 crystal) to subtract the background. The X-ray  
598 intensity was also measured on the pure Fe standard and a traditional k-ratio was calculated.  
599 When plotted against the Fe concentration, similarly to what has been obtained in the simpler  
600 case of the Fe  $K\alpha$  line by Keil and Fredriksson (1964), the k-ratios follow a smooth curve that  
601 can easily be fitted by a third order polynomial as seen on Figure 9. However, when the Fe  
602 concentration is plotted as a function of the experimental k-ratio, we were not able to obtain a  
603 satisfactory fit using established mathematical functions. The previously found third order  
604 polynomial cannot be inverted and used for practical application as it has two complex roots.  
605 With the help of a spreadsheet program, the fitting polynomial can easily be evaluated and  
606 tabulated for a large number of Fe concentrations, ranging from 0 to 100 wt%, with a small given  
607 step (e.g., 0.5 Fe wt%). The unknown k-ratio and the corresponding Fe concentration can then  
608 be obtained by linear interpolation of the closest values found in the spreadsheet. The obtained

609 third order polynomials are varying slowly with the k-ratio and thus a linear interpolation is a  
610 good approximation of the searched values, as long as the tabulation step is small enough.

611

612 In agreement with the theory discussed in section “Theoretical derivation of area k-ratio”,  
613 these k-ratios are still dependent on the spectrometer efficiency. Hence, the obtained calibration  
614 curves are different for each spectrometer as shown on Figures 9a and 9b. However, the two  
615 spectrometers, Sp1 (LTAP or TAP crystal) and Sp2 (TAP crystal), give almost the same fitting  
616 curve as their instrumental broadening is very similar.

617

618 These “non-universal” calibration curves were obtained on the SXFiveFE and the SX51  
619 instruments. On the SXFiveFE microprobe, the curves were deduced from measurements  
620 performed on the two sets of olivine previously described in this paper. Only the first set of  
621 olivines was used to derive the curve on the SX51 instrument. The measurements were  
622 performed at 7 kV and 90 nA. The obtained curves were then used to re-quantify the Fe  
623 concentration in the olivines. The results, shown in Table IV and V, give satisfactory quantitation  
624 numbers. The highest average absolute deviation is seen for the synthetic fayalite samples where  
625 the predictions underestimate the nominal values up to 2.42 wt%. The determination of this peak  
626 maximum calibration curve, despite its “non-universal” character, is easier and less time  
627 consuming than the calibration curve obtained using the peak area. The only drawback is that it  
628 requires a calibration curve to be acquired for each spectrometer. The calibration curve gives  
629 good quantification results especially when using the high-counting rate PC0 crystal even despite  
630 the overlap with both the Fe  $L\beta$  X-ray line and the  $L_3$  absorption edge.

631 It is of historical interest that Castaing, the father of EPMA, proposed in his landmark  
632 1952 thesis (English translation in 1955) a simple version of what we show here: an "alpha  
633 correction factor" for simple binary compounds, which was developed in more practical detail a  
634 decade later by Ziebold and Ogilvie (1963) and ultimately into the Bence and Albee (1968)  
635 correction factors for geological materials.

636 This method is more convenient to use than the area k-ratio method, but it gives slightly  
637 less accurate quantitative results. The mean RSD (in absolute value and in percent) of the Fe data  
638 obtained on the SXFiveFE instrument is 1.58% and 2.63% when using the area k-ratio calibration  
639 curve and the peak maximum k-ratio calibration curve, respectively. The mean RSD for the  
640 SX51 instrument is almost identical for both methods (3.60% and 3.61% using the area k-ratio  
641 and peak maximum k-ratio calibration curves, respectively). The compromise in accuracy  
642 relative to the speed of acquisition may be acceptable for certain applications.

643

644

645

646

## IMPLICATIONS

647

648 The discovery that a simple calibration curve approach, employing the relatively high  
649 intensity Fe  $L\alpha$  and  $L\beta$  peak integrals, can be used as a platform-independent tool for low kV  
650 quantitative analysis is significant. It provides an easy-to-use method to quantify the iron L X-  
651 ray signal by applying a universal equation and utilizing an easily available standard material  
652 like pure iron metal. The only drawback, longer acquisition of one or multiple wavescans (we

653 recommend averaging of 2 or 3), is balanced by the significantly higher count rates relative to  
654 those of the Fe L $\ell$  line, thereby reducing the analytical statistical error.

655 While applying the calibration curve approach to only the net Fe L $\alpha$  peak maximum  
656 intensities improves ease and speed of acquisition, it requires re-evaluating the calibration curve  
657 for each spectrometer and requires having a set of olivine samples of known composition with  
658 Fe content covering the concentration range of interest.

659 Our technique is particularly suited to high spectral resolution, parallel channel X-ray  
660 detectors such as the SXES as they acquire the entire Fe L X-ray spectrum simultaneously. While  
661 their presence in laboratories is currently very sparse, they could play a more important role in  
662 the future, particularly for geoscientists.

663 Future lines of research may include investigating the robustness of the calibration curve  
664 approach at different accelerating voltages (e.g. 3, 5, and 10 kV) and different spectrometer  
665 takeoff angles. In addition, the exploration of other iron-rich systems (minerals and glasses)  
666 could determine whether their Fe L $\alpha$ +L $\beta$  area k-ratio might fall on the same curve, or different  
667 curves, or have no correlation with composition.

668 It may also be of interest to try to obtain the same calibration curve with an EDS as it  
669 should work if the takeoff angle is 40° and would expand the applicability of this quantification  
670 method to a wider audience.

671

672

673

## ACKNOWLEDGMENTS

674

675 We thank the following for providing a second set of olivines for testing the calibration curve:

676 Noriko Kita, Mike Spicuzza, Kohei Fukuda. The authors would like to thank the two reviewers  
677 for their detailed comments which helped make the manuscript more complete. Support for this  
678 research came from the National Science Foundation: EAR13-37156 (JHF), EAR15-54269  
679 (JHF) and EAR-1625422 (AVDH).

680

681

## REFERENCES

682

683 Anderson, C.A. (1967) The quality of x-ray microanalysis in the ultra-soft x-ray region. *British*  
684 *Journal of Applied Physics*, 18, 1033-1043.

685

686 Anderson, C.A., and Hasler, M.F. (1966) Extension of electron microprobe techniques to  
687 biochemistry by the use of long wavelength X-rays. In R. Castaing, P. Deschamps and J.  
688 Philibert, Eds., *Proceedings of the Fourth International Conference on X-ray Optics and*  
689 *Microanalysis*, p. 310-327. Hermann, Paris.

690

691 Barker, F., Wones, D.R., Sharp, W.N., and Desborough, G. A. (1975) The Pikes Peak  
692 batholith, Colorado Front Range, and a model for the origin of the gabbro—*anorthosite—*  
693 *syenite—potassic granite suite*. *Precambrian Research*, 2 (2), 97-160.

694

695 Barkshire, I., Karduck, P., Rehbach, W.P., and Richter, S. (2000) High-spatial-resolution low-  
696 energy electron beam X-ray microanalysis. *Microchimica Acta*, 132 (2-4), 113–128.

697

698 Bertin, E.P. (1975) *Principles and Practice of X-Ray Spectrometric Analysis*, 1079 p. Plenum  
699 Press, New York.

700

701 Buse, B., and Kearns, S. (2015) Importance of carbon contamination in high-resolution (FEG)  
702 EPMA of silicate minerals. *Microscopy and Microanalysis*. 21, 594-605.

703 doi:10.1017/S1431927615000288

704

705 Buse, B., and Kearns, S. (2018) Quantification of Olivine Using Fe L $\alpha$  in Electron Probe  
706 Microanalysis (EPMA). *Microscopy and Microanalysis*. 24, 1–7. doi:

707 10.1017/S1431927618000041

708

709 Castaing, R. (1952) Application des sondes électroniques à une méthode d'analyse ponctuelle  
710 chimique et cristallographique. Ph.D. thesis, Université de Paris, France. (Publication ONERA  
711 no. 55)

712

713 Castaing, R. (1955) Application of Electron Probes to Local Chemical and Crystallographic  
714 Analysis (Application des sondes électroniques à une méthode d'analyse ponctuelle chimique  
715 et cristallographique). Translation by Pol Duwez and David B. Wittry, California Institute of  
716 Technology. (download [http://www.microprobe.org/history/Castaing-Thesis-  
717 clearscan.pdf/view](http://www.microprobe.org/history/Castaing-Thesis-clearscan.pdf/view))

718

719 Castaing, R. (1960) Electron Probe Microanalysis. In M. Marton, Ed., *Advances in Electronics  
720 and Electron Physics*, p. 317-386. Academic Press Inc., New York and London.

721



- 722 Castaing, R., and Fredriksson, K. (1958) Analyses of cosmic spherules with an X-ray  
723 microanalyser. *Geochimica et Cosmochimica Acta*, 14, 114-117.  
724
- 725 Donovan, J., Kremser, D., Fournelle, J., and Goemann, K. (2018). Probe for Windows User's  
726 Guide and Reference, Enterprise Edition, Probe Software, Inc., Eugene, OR.  
727
- 728 Duncumb, P. (1960) Improved resolution with X-ray scanning microanalyser. In A. Engstrom,  
729 V. Cosslett, and H. Pattee, Eds., *X-ray Microscopy and X-ray Microanalysis*, Proceedings of  
730 2nd International Symposium, p. 365-371. Elsevier, Amsterdam.  
731
- 732 Fialin, M., Wagner, C., and Pascal, M.-L. (2011) Iron speciation using electron microprobe  
733 techniques: application to glassy melt pockets within a spinel lherzolite xenolith. *Mineralogical*  
734 *Magazine*, 75, 347–362.  
735
- 736 Finch, C.B., Clark, G.W., and Kopp, O.C. (1980) Czochralski growth of single-crystal fayalite  
737 under controlled oxygen fugacity conditions. *American Mineralogist*, 65, 381–389.  
738
- 739 Fournelle, J.H. (1988) *The Geology and Petrology of Shishaldin Volcano, Unimak Island,*  
740 *Aleutian Islands*; Ph.D. Thesis, The Johns Hopkins University, Baltimore.  
741
- 742 Fournelle, J.H., Kim, S., and Perepezko, J.H. (2005) Monte Carlo simulation of Nb  $K\alpha$   
743 secondary fluorescence in EPMA: comparison of PENELOPE simulations with experimental  
744 results. *Surface and Interface Analysis*, 37, 1012-1016.

745

746 Fournelle, J., Cathey, H., Pinard, P.T., and Richter, S. (2016) Low voltage EPMA: experiments  
747 on a new frontier in microanalysis - analytical lateral resolution. In IOP Conference Series:  
748 Materials Science and Engineering, 109, 1, p. 012003. IOP Publishing.

749

750 Gopon, P., Fournelle, J., Sobol, P.E., and Llovet, X. (2013) Low-Voltage Electron-Probe  
751 Microanalysis of Fe–Si Compounds Using Soft X-Rays. *Microscopy and Microanalysis*, 19,  
752 1698-1708.

753

754 Heinrich, K.F.J. (1987) Mass absorption coefficients for electron probe microanalysis. In J.D.  
755 Brown and R.H. Packwood, Eds., *Proceedings of the 11th international congress on X-ray*  
756 *optics and microanalysis*, p. 67–119. University of Western Ontario Press, London, Ontario.

757

758 Höfer, H.E., Brey, G.P., Schulz-Dobrick, B., and Oberhansli, R. (1994) The determination of  
759 the oxidation state of iron by the electron microprobe. *European Journal of Mineralogy*, 6, 407-  
760 418.

761

762 Hovington, P., Drouin, D., and Gauvin, R. (1997a) CASINO: A new Monte Carlo code in C  
763 language for electron beam interaction—Part I: Description of the program. *Scanning*, 19, 1-  
764 14.

765

- 766 Hovington, P., Drouin, D., Gauvin, R., and Joy, D.C. (1997b) Parameterization of the range of  
767 electrons at low energy using the CASINO Monte Carlo program. *Microscopy and*  
768 *Microanalysis*, 3, 885-886.
- 769
- 770 International Organization for Standardization (2003) Microbeam analysis — Electron probe  
771 microanalysis — Guidelines for the determination of experimental parameters for wavelength  
772 dispersive spectroscopy (ISO 14594).
- 773
- 774 Jarosewich, E., Nelen, J.A., and Norberg, J.A. (1980) Reference samples for electron  
775 microprobe analysis. *Geostandards Newsletter*, 4(1), 43-47.
- 776
- 777 Kearns, S., Buse, B., and Wade, J. (2014) Mitigating thermal beam damage with metallic coats  
778 in low voltage FEG-EPMA of geological materials. *Microscopy and Microanalysis*, 20(S3),  
779 740-741.
- 780
- 781 Keil, K., and Fredriksson, K. (1964) The iron, magnesium, and calcium distribution in  
782 coexisting olivines and rhombic pyroxenes of chondrites. *Journal of Geophysical Research*,  
783 69(16), 3487-3515.
- 784
- 785 Li, X., Zhang, C., Almeev, R.R., Zhang, X.-C., Zhao, X.-F., Wang, L.-X., Koepke, J., and  
786 Holtz, F. (2019) Electron probe microanalysis of Fe<sup>2+</sup>/ΣFe ratios in calcic and sodic-calcic  
787 amphibole and biotite using the flank method. *Chemical Geology*, 509, 152–162.
- 788

789 Libourel, G., and Portail, M. (2018) Chondrules as direct thermochemical sensors of solar  
790 protoplanetary disk gas. *Science advances*, 4(7), p.eaar3321.

791

792 Llovet, X., and Galan, G. (2003) Correction of secondary X-ray fluorescence near grain  
793 boundaries in electron microprobe analysis: Application to thermobarometry of spinel  
794 lherzolites. *American Mineralogist*, 88, 121-130.

795

796 Llovet, X., and Merlet, C. (2010) Electron Probe Microanalysis of Thin Films and Multilayers  
797 Using the Computer Program XFILM. *Microscopy and Microanalysis*, 16, 21-32.

798

799 Llovet, X., and Salvat, F. (2016) PENEPMA: a Monte Carlo programme for the simulation of  
800 X-ray emission in EPMA. In *IOP Conference Series: Materials Science and Engineering*, 109,  
801 1, p. 012009. IOP Publishing.

802

803 Llovet, X., Heikinheimo, E., Galindo, A.N., Merlet, C., Bello, J.A., Richter, S., Fournelle, J.,  
804 and Van Hoek, C.J.G. (2012) An inter-laboratory comparison of EPMA analysis of alloy steel  
805 at low voltage. In *IOP Conference Series: Materials Science and Engineering*, 32, 1, p. 012014.  
806 IOP Publishing.

807

808 Llovet, X., Pinard, P.T., Heikinheimo, E., Louhenkilpi, S., and Richter, S. (2016) Electron  
809 probe microanalysis of Ni silicides using Ni-L X-ray lines. *Microscopy and Microanalysis*, 22,  
810 1233-1243.

811

- 812 McSwiggen, P. (2014) Characterisation of sub-micrometre features with the FE-EPMA. In IOP  
813 Conference Series: Materials Science and Engineering, 55, 1, p. 012009. IOP Publishing.  
814
- 815 Merlet, C., and Llovet, X. (2012) Uncertainty and capability of quantitative EPMA at low  
816 voltage – A review. In IOP Conference Series: Materials Science and Engineering, 32, 1, p.  
817 012016. IOP Publishing.  
818
- 819 Moy, A., Fournelle, J.H., and von der Handt, A. (2019) Quantitative measurement of iron-  
820 silicides by EPMA using the Fe  $L\alpha$  and  $L\beta$  X-ray lines: a new twist to an old approach.  
821 Microscopy and Microanalysis, in press. doi: 10.1017/S1431927619000436.  
822
- 823 Pinard, P.T., and Richter, S. (2016) Quantification of low concentration elements using soft X-  
824 rays at high spatial resolution. In IOP Conference Series: Materials Science and Engineering,  
825 109, 1, p. 012013. IOP Publishing  
826
- 827 Pouchou, J.L. (1996) Use of soft X-rays in microanalysis. Mikrochimica Acta 13(Suppl), 39–  
828 60.  
829
- 830 Pouchou, J.L., and Pichoir, F. (1991) Quantitative analysis of homogeneous or stratified  
831 microvolumes applying the model “PAP”, In K. F. J. Heinrich and D. E. Newbury, Eds.,  
832 Electron Probe Quantitation, p. 31-75. Plenum Press, New York.  
833

- 834 Reed, S.J.B. (1966) Spatial resolution in electron probe microanalysis. In R. Castaing, P.  
835 Deschamps and J. Philibert, Eds., Proceedings of the Fourth International Conference on X-ray  
836 Optics and Microanalysis, p. 339-349. Hermann, Paris.  
837
- 838 Reed, S.J.B. (1975) Electron Microprobe Analysis. Cambridge University Press, Cambridge.  
839
- 840 Ritchie, N.W. (2011) Getting Started with NIST DTSA-II. *Microscopy Today*, 19(1), 26-31.  
841
- 842 Rose, T. R., Sorensen, S.S., and Post, J.E. (2009) The impurities in the Rockport fayalite  
843 microbeam standard: How bad are they? American Geophysical Union, Fall Meeting 2009,  
844 abstract id. V31E-2008.  
845
- 846 Salvat, F., Fernandez Varea, J.M., and Sempau, J. (2013) PENELOPE - A code system for  
847 Monte Carlo Simulation of Electron and Photon Transport. OECD/Nuclear Energy Agency,  
848 Issy-les-Moulineaux, France.  
849
- 850 Saunders, K., Buse, B., Kilburn, M.R., Kearns, S., and Blundy, J. (2014) Nanoscale  
851 characterisation of crystal zoning. *Chemical Geology*, 364, 20-32.  
852
- 853 Shea, T., Lynn, K.J., and Garcia, M.O. (2015) Cracking the olivine zoning code:  
854 Distinguishing between crystal growth and diffusion. *Geology*, 43, 935–938. doi:  
855 10.1130/G37082.1.  
856

- 857 Terauchi, M., and Sato, Y. (2018) Chemical State Analyses by Soft X-ray Emission  
858 Spectroscopy. JEOL NEWS, 53(1), 30-35.
- 859
- 860 Terauchi, M., Takahashi, H., Handa, N., Murano, T., Koike, M., Kawachi, T., Imazono, T.,  
861 Hasagawa, N., Koeda, M., Nagano, T., and Sasai, H. (2011) An extension up to 4 keV by a  
862 newly developed multilayer-coated grating for TEM-SXES spectrometer. Microscopy and  
863 Microanalysis, 17(S2), 604-605.
- 864
- 865 Vladár, A.E., and Postek, M.T. (2009) The Scanning Electron Microscope. In J. Orloff, Ed.,  
866 Handbook of Charged Particle Optics, 2nd ed., p. 437-496. CRC Press.
- 867
- 868 Zschornack, G.H. (2007) Handbook of X-Ray Data. Springer-Verlag, Berlin.
- 869
- 870

871 **Figure captions**

872 **Figure 1. (a)** SE image of an 800 nanometer iron oxide crystal in K409 silicate glass. A profile  
873 is drawn across a crystal edge to calculate the "edge resolution" based on the change in signal  
874 intensity.

875 **(b)** Edge resolution, determined by fitting the signal intensity profile with an error function.  
876 Depending upon the preferred convention of the degree of relative intensity change, various  
877 beam diameters may be calculated.

878

879 **Figure 2.** PENEPMA simulated vertical cross sections for Mg K $\alpha$  X-rays generated at depth in  
880 Fo80 olivine, with both 15 kV W-filament (210 nm diameter, **left**) and FE beam (35 nm diameter,  
881 **right**). Beam diameter values for 20 nA beam currents use estimates given in McSwiggen (2014)  
882 and Pinard and Richter (2016). Outer contour shows the bounding perimeter where generation  
883 of Mg K $\alpha$  X-rays drops to 1% of the maximum generated intensity; internal contours are for  
884 10%, 20%, 30% ... Mg K $\alpha$  X-ray generation. Matrix absorption effect on the generated Mg K $\alpha$   
885 X-rays is not included.

886

887 **Figure 3.** PENEPMA simulated vertical cross sections for Mg K $\alpha$  X-rays generated at depth in  
888 Fo80 olivine, with both 7 kV W-filament (210 nm diameter, **left**) and FE beam (35 nm diameter,  
889 **right**). Both FE and tungsten sources show much reduced zones of Mg K $\alpha$  X-ray generation  
890 with depth compared to the 15 kV simulations (Figure 2). Note: these are models of X-ray  
891 generation and do not take into account matrix absorption.

892



893 **Figure 4.** Quantification of the first set of olivine samples using the traditional quantification  
894 method and the Fe  $L\alpha$  X-ray line at 7 kV. Three Fe standards were used to perform the  
895 quantification. Regardless of the standard used, large deviations from the nominal Fe  
896 concentration are observed.

897

898 **Figure 5.** Integrated Fe  $L\alpha+L\beta$  k-ratios acquired at 7 kV on two different instruments with six  
899 different spectrometers. The olivine peak area measurements were normalized to the peak area  
900 value obtained on the pure Fe standard.

901

902 **Figure 6.** Calibration curve obtained by measuring the Fe  $L\alpha$  and  $L\beta$  spectra at 7 kV on all  
903 olivine samples and averaging the results. The area k-ratio has been obtained relative to the pure  
904 Fe sample by integrating the Fe  $L\alpha-L\beta$  spectrum (area method). (Error bars representing the  
905 standard deviation of the experimental data are also plotted).

906

907 **Figure 7.** Quantification of the first set of olivine samples using the calibration curve (Eq. 1)  
908 determined at 7 kV. The measurements were performed on the SX51 instrument using three  
909 different WDSs.

910

911 **Figure 8.** Quantification of a second set of olivine samples using the calibration curve (Eq. 1) at  
912 7 kV. The measurements were performed on the SXFiveFE microprobe with three different  
913 WDSs.

914

915 **Figure 9.** Calibration curves based on the maximum net peak intensity of the Fe L $\alpha$  X-ray line  
916 acquired with the SXFiveFE (**a**) and SX51 (**b**) microprobes. The curves obtained for the LTAP  
917 (continuous line) and TAP (dashed line) crystals are very similar.  
918  
919

920 **Footnote**

921 <sup>1</sup> The physical terms kV and keV are used here in the strict sense: kV refers to an electrical  
922 potential (as between the cathode and anode of the source), whereas keV refers to an energy of  
923 a "particle" such as an electron or photon.

924

925 **Tables**

926 **Table I.** Oxide composition (wt%) of olivines, measured at 15 kV using the traditional K $\alpha$  lines  
927 with the CAMECA SX51 instrument. The elemental Fe concentration is also given in the last  
928 column. Numbers in parenthesis are the estimated standard deviations (uncertainties on the last  
929 digits).

	SiO <sub>2</sub> (wt%)	FeO (wt%)	MnO (wt%)	MgO (wt%)	CaO (wt%)	Total (wt%)	Fe (wt%)
Synthetic Fayalite	28.79(13)	69.35(48)	0.20(4)	0.02(1)	0.00(2)	98.36(50)	53.90(31)
Wards Fayalite	29.31(19)	64.89(60)	4.49(38)	0.50(7)	0.09(4)	99.29(74)	50.44(30)
SH111	34.44(15)	41.93(43)	0.86(5)	21.10(11)	0.22(1)	98.55(47)	32.59(24)
SH11	34.96(25)	38.80(55)	0.86(5)	24.26(22)	0.26(2)	99.15(64)	30.16(24)
SH25	36.34(24)	33.89(98)	0.69(6)	28.66(73)	0.25(3)	99.83(1.25)	26.34(22)
SH9	37.49(20)	27.33(35)	0.57(5)	34.21(28)	0.18(1)	99.78(49)	21.25(20)
SH15	38.77(28)	23.98(39)	0.38(3)	38.09(30)	0.19(2)	101.41(56)	18.64(19)
USNM Springwater	39.82(20)	16.90(2)	0.32(11)	43.64(2)	0.02(17)	100.70(29)	13.14(16)
USNM San Carlos	40.95(25)	9.62(23)	0.14(4)	48.93(28)	0.10(2)	100.10(44)	7.64(12)

930

931

932 **Table II.** Re-quantification of the first set of olivine samples with the area k-ratio calibration  
 933 curve using different positions and different grains. The measurements were performed at 7 kV  
 934 and 90 nA with the SX51 microprobe using three different WDSs. Numbers in parenthesis are  
 935 the estimated standard deviations (uncertainties on the last digits).

Sample name	Fe concentration (wt%)			
	Nominal	Sp1 (TAP)	Sp2 (TAP)	SP4 (PC0)
Coarse San Carlos Mnt 61	7.75(12)	7.46	7.38	7.17
SH15 small Fo88.3 Mnt 62	9.57(41)	7.99	7.71	8.30
USNM Springwater #2	13.20(7)	12.95	13.02	13.19
USNM Springwater #1	13.22(19)	12.72	13.21	13.16
SH15 Big Fo72.7 Mnt 62	19.01(12)	17.08	15.7	18.28
SH11 #7 core Fo72	19.79(25)	19.67	18.7	20.14
SH9 Fo67.6 Mnt 62	21.35(16)	21.46	20.58	21.43
SH11 small Fo64	23.65(17)	23.86	23.70	24.12
SH9 Fo62.6 Mnt 62	24.66(13)	24.19	23.83	24.46
SH11 #11 small Fo52	30.21(18)	30.31	29.21	29.36
Wards Fayalite Mnt 61	50.79(23)	48.26	48.21	51.48
Rockport Fayalite Mnt 30	52.27(23)	48.33	47.79	50.23
Synthetic Fayalite Mnt 61	54.55(33)	52.03	53.48	55.00
Fe metal #1	100.0	99.98	99.99	100.00
Fe metal #2	100.0	100.00	100.00	99.99

936  
 937

938 **Table III.** Quantification of a second set of olivines at 7 kV and 90 nA using the area k-ratio  
 939 calibration curve with the SXFiveFE microprobe and three WDSs. Nominal refers to the 15 kV  
 940 measurements using the traditional Fe K $\alpha$  X-ray line. Numbers in parenthesis are the estimated  
 941 standard deviations (uncertainties on the last digits).

Sample name	Fe concentration (wt%)			
	Nominal	Sp1 (LTAP)	Sp2 (TAP)	SP4 (PC0)
WKOL #1	4.11(14)	3.92	4.34	3.54
HaKOL g3 #8	5.98(6)	6.22	6.32	5.44
UWOL-1 #4	7.94(4)	8.01	8.64	7.19
SWOL-1 #2	13.22(8)	13.05	13.71	12.63
SWOL-1 #2 ROM	13.22(8)	13.67	14.00	12.97
KNOL-2 #6	15.44(11)	15.41	15.60	14.04
FJOL #5	18.76(8)	18.68	18.62	18.04
OROL #20	26.78(4)	26.88	26.77	25.93
Rockport Fayalite Mnt 30				
Rand	52.50(23)	51.74	50.48	52.29
Synthetic Fayalite Mnt 61				
(new pos)	54.80(33)	53.44	52.98	52.24
Fe metal	100.0	99.99	99.99	99.99

942  
 943

944 **Table IV.** Re-quantification of the Fe concentration of the two sets of olivines using the  
 945 calibration curves obtained using the Fe L $\alpha$  peak maximum. The results were obtained at 7 kV  
 946 and 90 nA with the SXFiveFE microprobe and three WDSs. Numbers in parenthesis are the  
 947 estimated standard deviations (uncertainties on the last digits).

	Fe concentration (wt%)			
		SXFiveFE		
Sample name	Nominal	Sp1 (LTAP)	Sp2 (TAP)	Sp4 (PC0)
First olivine set				
USNM San Carlos	7.64(12)	7.38	7.73	7.23
USNM Springwater	13.14(16)	12.75	12.63	12.57
SH15	18.64(19)	19.56	18.55	18.88
SH9	21.25(20)	22.24	21.98	21.53
SH25	26.34(22)	28.01	28.51	26.45
SH11	30.16(24)	31.75	31.08	30.89
SH111	32.59(24)	35.06	33.25	33.07
Wards Fayalite	50.44(30)	50.74	51.39	49.99
Synthetic Fayalite	53.90(31)	52.43	52.19	53.03
Fe metal	100.0	99.60	99.60	99.55
Second olivine set				
WKOL #1	4.11(14)	3.98	3.85	4.16
HaKOL g3 #8	5.98(6)	5.86	5.98	6.37
UWOL-1 #4	7.94(4)	7.52	7.41	8.22

SWOL-1 #2	13.22(8)	13.05	13.43	13.98
KNOL-2 #6	15.44(11)	13.41	14.19	14.66
FJOL #5	18.76(8)	17.95	18.50	18.95
OROL #20	26.78(4)	26.49	27.30	27.59
Rockport Fayalite Mnt 30				
Rand	52.50(23)	51.74	51.41	52.03
Synthetic Fayalite Mnt 61				
(new pos)	54.80(33)	52.81	53.18	53.55
Fe metal	100.0	99.60	99.60	99.55

948

949

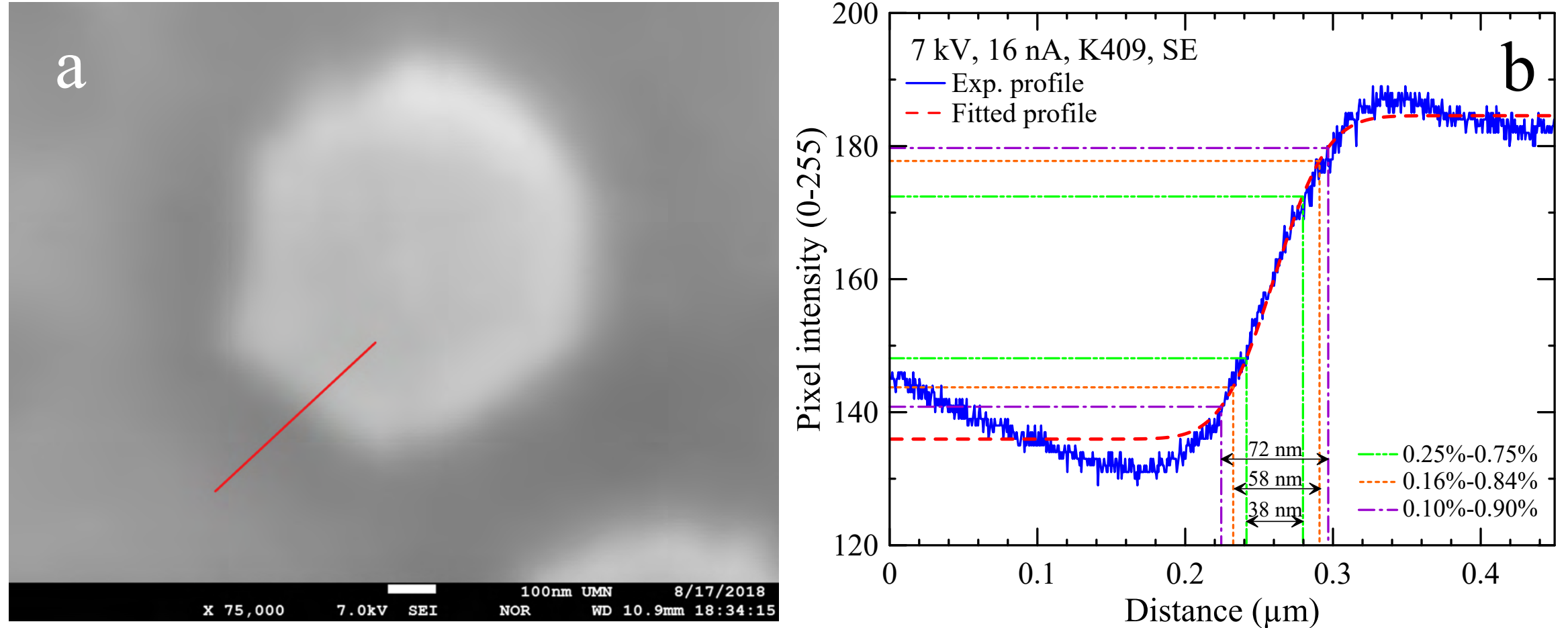


950 **Table V.** Reevaluation of the Fe concentration of the first set of olivines using the calibration  
 951 curves obtained using the Fe L $\alpha$  peak maximum. The results were obtained at 7 kV and 90 nA  
 952 with the SX51 microprobe and three WDSs. Numbers in parenthesis are the estimated standard  
 953 deviations (uncertainties on the last digits).

Sample name	Fe concentration (wt%)			
		SX51		
First olivine set	Nominal	Sp1 (TAP)	Sp2 (TAP)	Sp4 (PC0)
Coarse San Carlos	7.46(77)	6.94	6.98	7.13
USNM Springwater	13.20(7)	11.52	12.08	12.43
SH11 Fo72	19.79(25)	19.26	19.02	19.80
SH9 Fo67	21.70(30)	21.43	20.77	21.46
SH111 Fo47 #1	32.12(22)	33.69	33.90	33.30
SH111 Fo47 #2	32.12(22)	33.76	33.39	33.08
SH111 Fo47 #3	32.12(22)	33.69	33.90	33.30
Wards Fayalite	50.90(39)	50.02	49.67	49.91
Rockport Fayalite	52.29(26)	52.03	52.07	51.52
Synthetic Fayalite	54.55(33)	52.18	52.56	53.17
Fe metal	100.0	99.61	99.61	99.56

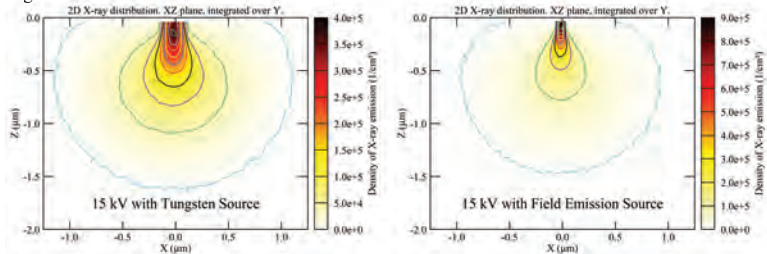
954

# Figure 1



This is a preprint, the final version is subject to change, of the American Mineralogist (MSA)  
Cite as Authors (Year) Title. American Mineralogist, in press.  
DOI: <https://doi.org/10.2138/am-2019-6865>

Figure 2



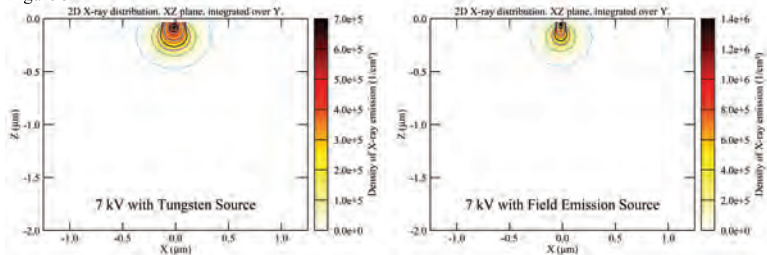
Always consult and cite the final, published document. See <http://www.minsocam.org> or GeoscienceWorld

This is a preprint, the final version is subject to change, of the American Mineralogist (MSA)

Cite as Authors (Year) Title. American Mineralogist, in press.

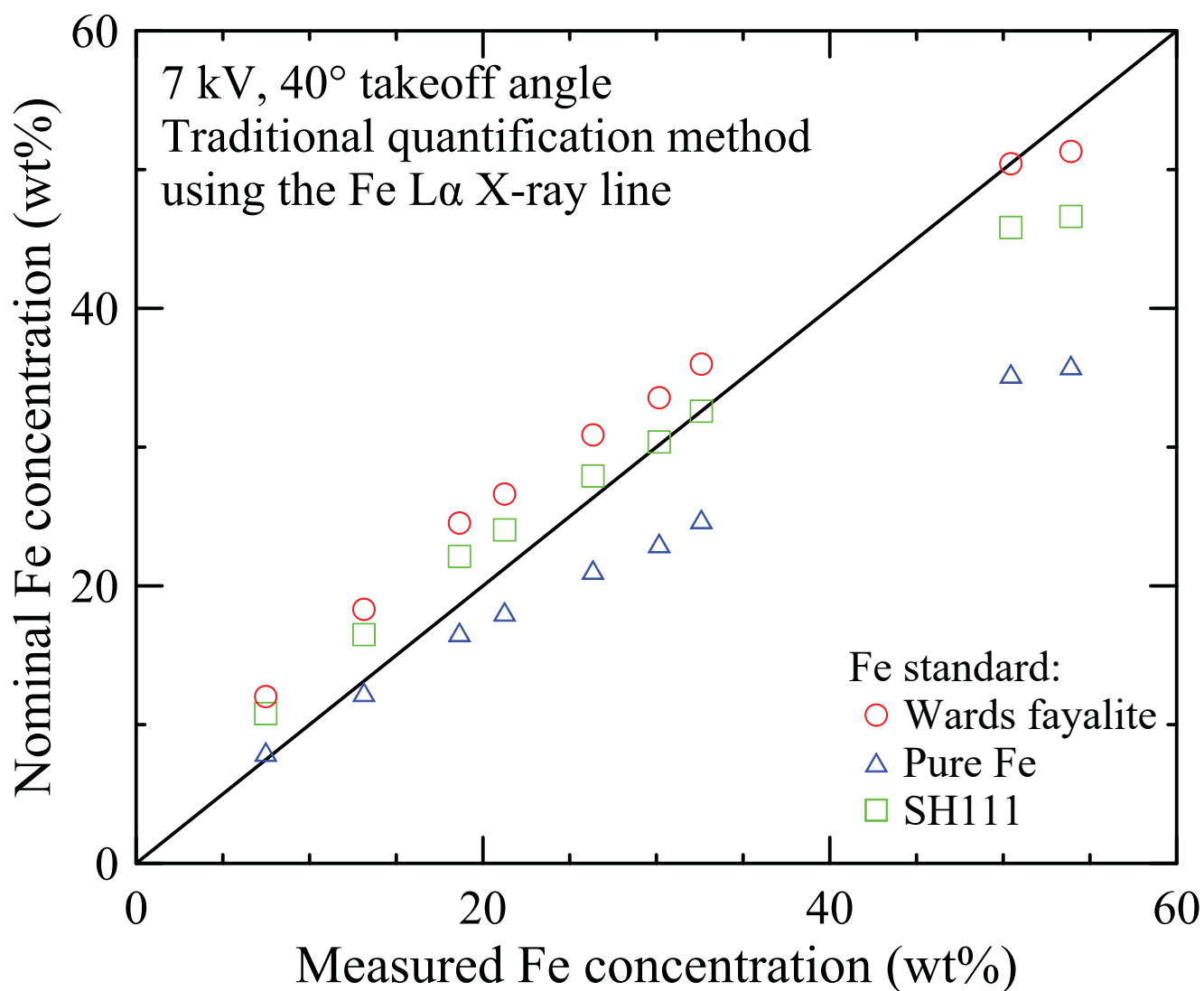
DOI: <https://doi.org/10.2138/am-2019-6865>

Figure 3



Always consult and cite the final, published document. See <http://www.minsocam.org> or GeoscienceWorld

# Figure 4



# Figure 5

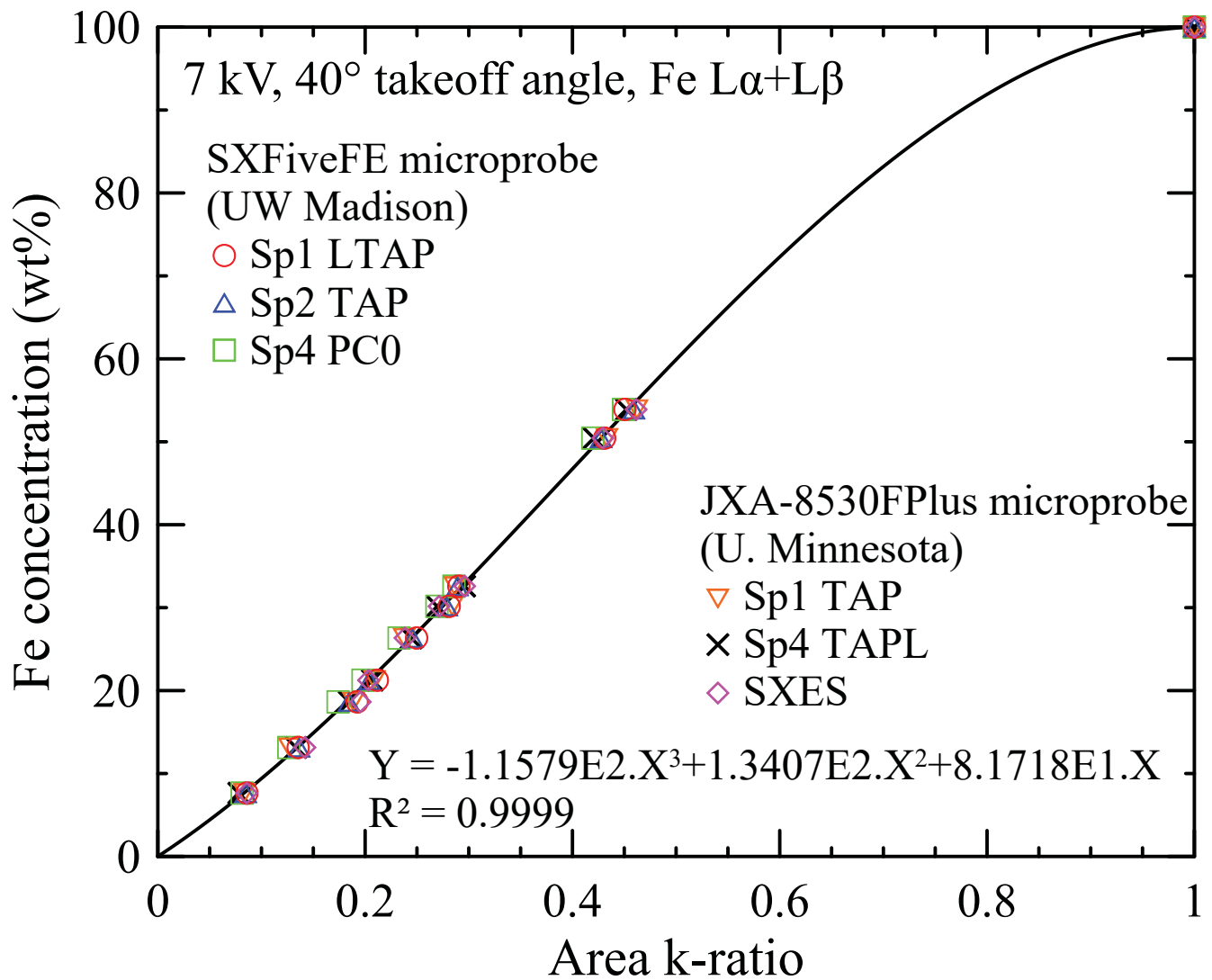


# Figure 6

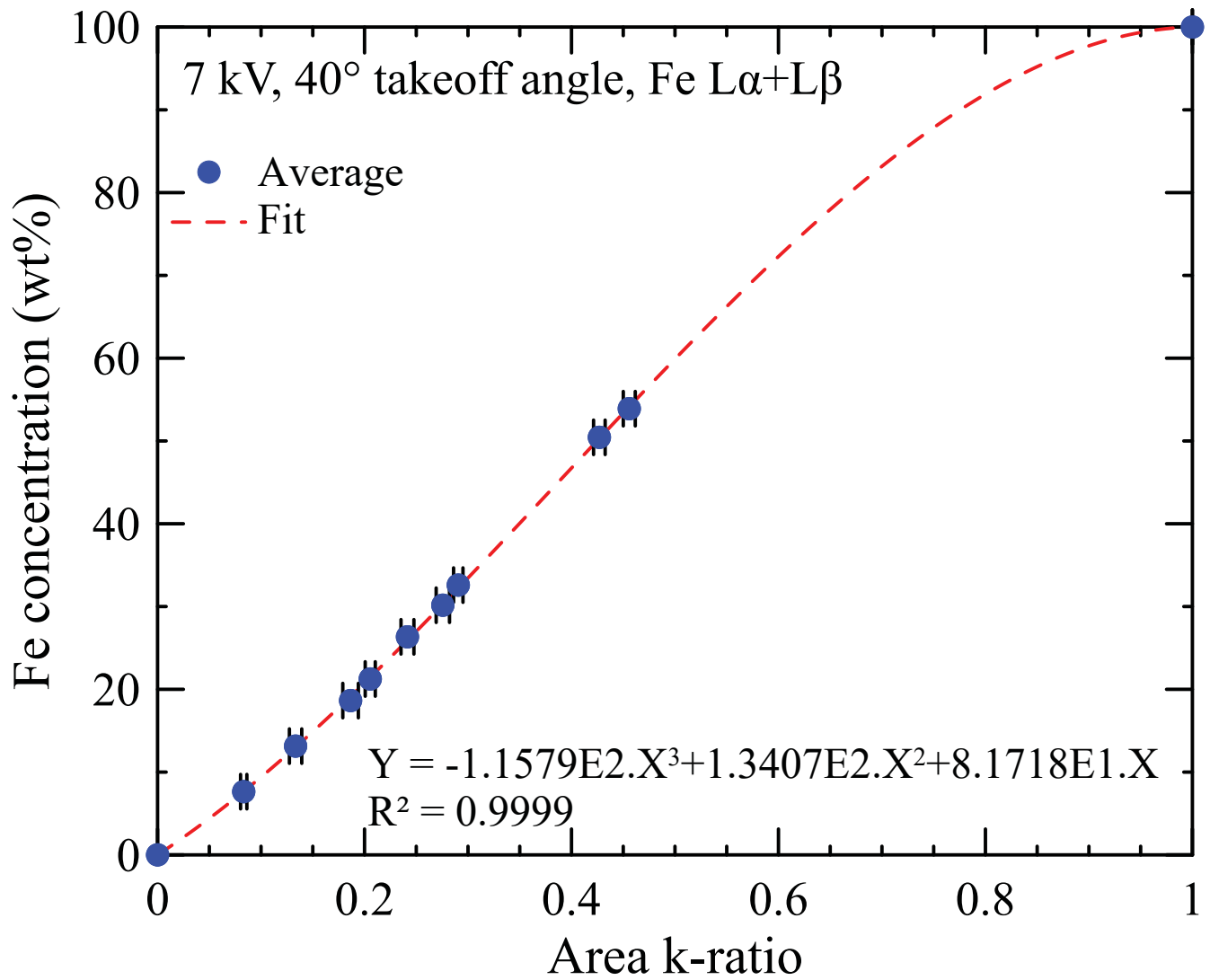


# Figure 7

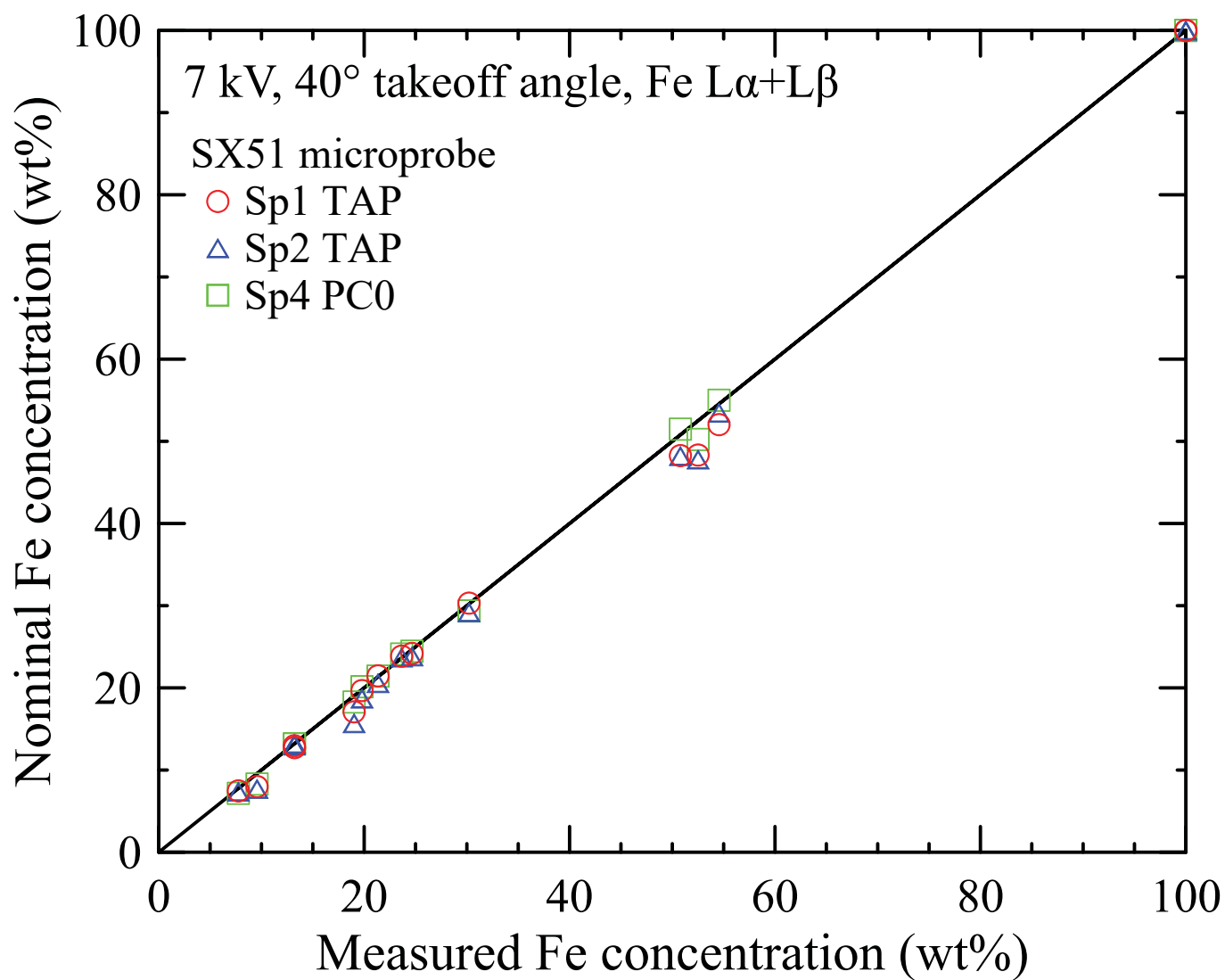




## Figure 8

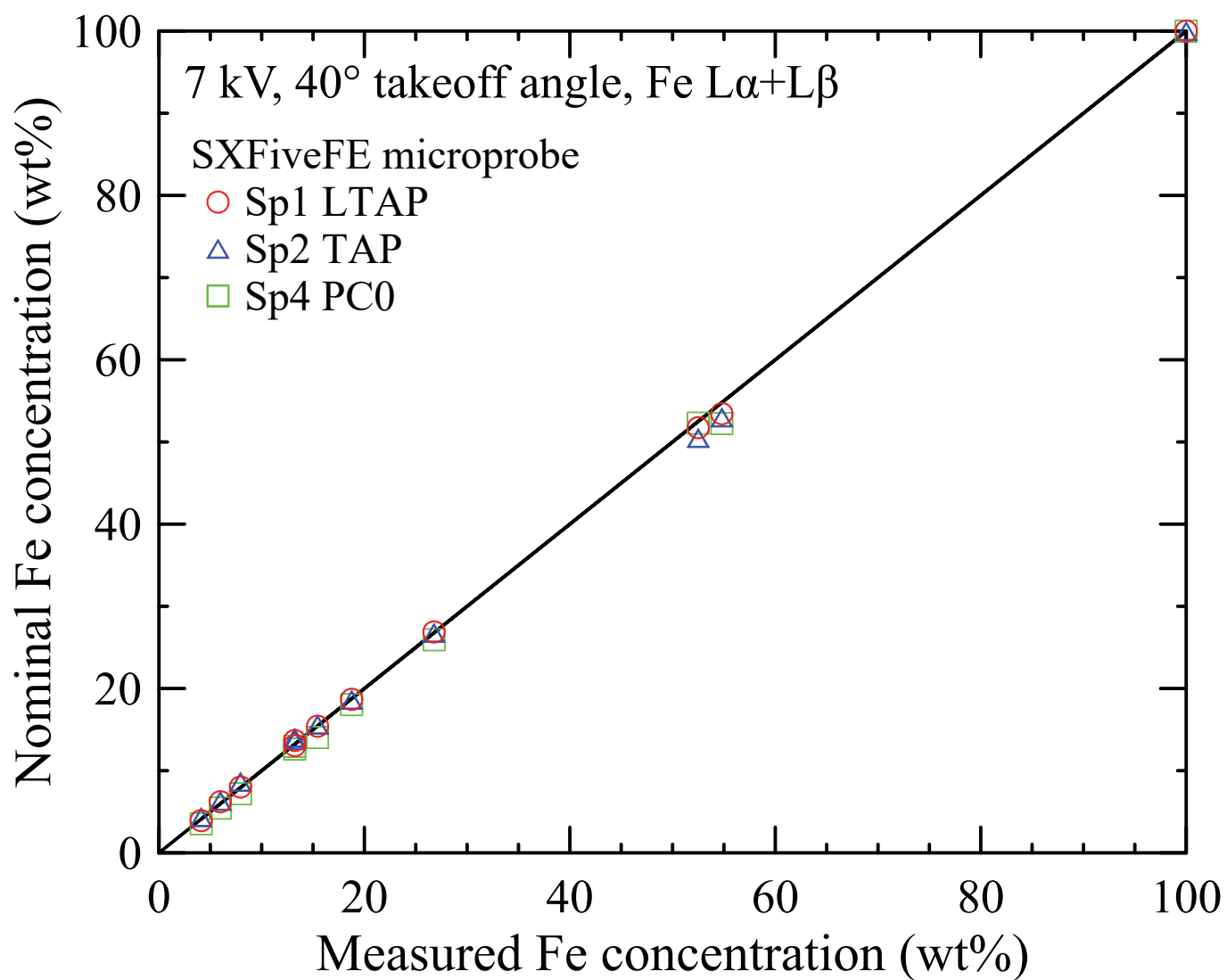


# Figure 9

